ADVANCED FUNCTIONAL MATERIALS

DOI: 10.1002/adfm.200700506

Synthesis and Performance of $BaAl_2O_4$ with a Wide Spectral Range of Optical Absorption**

By *Li-wu Zhang*, *Li Wang*, and *Yong-fa Zhu**

Oxygen-deficient $BaAl_2O_4$, with strong optical absorption in the spectra range from 200 to 2500 nm, was prepared by a simple and economic thermal treatment of $BaAl_2O_4$ in a H_2 gas flow. Further studies found that a molar ratio of oxygen vacancies of about 0.4 % existed in the prepared oxygen-deficient $BaAl_2O_4$ sample. The influence of oxygen vacancies on the electronic band structures and optical absorption of $BaAl_2O_4$ are elucidated via first principle calculations. Oxygen vacancies introduce impurity states above the valence band; these impurities expand and enhance the optical absorption of $BaAl_2O_4$. This approach is proposed to develop a new type of optical materials and to be applicable to many wide bandgap materials.

1. Introduction

Wide spectral range photoabsorptive materials are of considerable interest because of their potential applications in optical data processing, photodynamic therapy, photodetection, solar energy utilization, and military camouflage.[1,2] The materials that can show strong absorption in the near-IR (NIR) region include Ni^{II}-dithiolene complexes, some mixed-valence complexes, molecules with extended conjugated systems, and some conducting polymers.[2–6] However, as far as we know, no material has been reported to show strong absorption in the UV, visible light, and NIR regions.

The photoabsorption performance of materials can be enhanced or expanded by introducing defects.[7–9] Defect-related properties have been widely investigated in semiconductors, such as Si,[10] TiO_2,[11] ZnO,[12] and $PbWO_4$.[13] The first-principle calculation, electron-spin resonance (ESR) spectroscopy, and temperature-programmed reduction (TPR) analysis show that photoabsorption in the visible region of the reduced TiO_2 can be attributed to oxygen vacancies caused by the reduction.[13–16] However, these semiconductors usually have a simple defect structure, while the optical absorption of insulating metal oxides has seldom been reported. The highly ionic nature of some materials, especially MgO, BaO, and Al_2O_3, allows the formation of many stable defect sites, including edges, corners, and anion/cation vacancies. Metal oxide insulators with a wide forbidden band and more complex defect structures may obtain wide-range photoabsorption and have more promising applications. In this work, we attempt to enhance and expand the photoabsorption of $BaAl_2O_4$ by introducing defects.

$BaAl_2O_4$, which belongs to the family of stuffed tridymites, is a high-melting-point material with good dielectric, pyroelectric, and hydraulic-hardening properties. It has been studied for coating and refractory cement applications.[17–21] $BaAl_2O_4$ is also notable for its good luminescent performance.[22,23] In our previous work, a simple method to prepare nanometer-sized $BaAl_2O_4$ have been developed.[24] In the present work, a $BaAl_2O_4$ sample with excellent photoabsorption from UV to near-IR was obtained via a simple and economic thermal treatment in H_2. Such strong and uniform absorption in a wide spectral range has never been reported before, to the best of our knowledge; it could have promising applications in many fields, such as in the utilization of solar energy, military camouflage coatings, and so on. Also, in order to understand the photoabsorption mechanisms, experimental and theoretical studies have been performed. The prepared oxygen-deficient $BaAl_2O_4$ sample contained about a 0.4 % molar ratio of oxygen vacancies. Theoretical calculations proved that oxygen vacancies could actually enhance and expand the optical absorption performance of the $BaAl_2O_4$ sample.

2. Results and Discussion

2.1. Optical Properties of Defected $BaAl_2O_4$

Nanometer-sized $BaAl_2O_4$ particles were synthesized by using an amorphous heteronuclear complex as a precursor, as demonstrated in our previous report.[24] The defect structure of $BaAl_2O_4$ was obtained by a thermal treatment in a H_2 flow at given temperatures for several hours. The UV-vis spectrum of

[*] Prof. Y.-F. Zhu, Dr. L.-W. Zhang, Dr. L. Wang
Department of Chemistry, Tsinghua University
Beijing 100084 (P.R. China)
E-mail: zhuyf@mail.tsinghua.edu.cn

[**] This work was supported by the Chinese National Science Foundation (20433010, 20571047). Supporting Information is available online from Wiley InterScience or from the author; included in the Supporting Information is the band structure of $BaAl_2O_{4-x}$ with $x = 0.0$ and 0.08, the PDOS of Ba, Al, and O atoms in $BaAl_2O_4$, optical absorption spectra of micrometer-sized $BaAl_2O_4$ before and after reduction, the C 1s X-ray photoelectron spectra of $BaAl_2O_4$ samples before and after reduction, and FTIR spectra of $BaAl_2O_4$ before and after reduction.

$BaAl_2O_4$ is given in Figure 1A and shows a very low absorption (only 7 %) in the light range from UV to NIR, and no specific absorption peaks were observed. After the $BaAl_2O_4$ sample was reduced by H_2 at 700 °C for 2 h, a very strong absorption in the wavelength range from 200 to 2500 nm appeared. About 90 % of the light was absorbed, based on the UV-vis spectrum. To confirm this result, the preparation and measurement experiments were repeated many times, and the same results were obtained. Additionally, a 1 % (by molar ratio) Eu^{3+}-doped $BaAl_2O_4$ sample was reduced by H_2 at 700 °C for 2 h and a similar result was obtained to that of the R-$BaAl_2O_4$ sample ("R" represents the reduced $BaAl_2O_4$). No characteristic absorption peak of Eu^{3+} or Eu^{2+} was observed, but a slight enhancement of the photoabsorption was found.

Moreover, to prove the applicability of this method to obtain material with special optical properties, the same research was carried out on another material, $SrAl_2O_4$, which shares similar physical and chemical properties with $BaAl_2O_4$. A similar optical performance was observed in the reduced $SrAl_2O_4$ sample, as shown in Figure 1B.

2.2. The Oxygen-Deficient Structure in $BaAl_2O_4$

The crystalline structure of the $BaAl_2O_4$ and R-$BaAl_2O_4$ samples was determined by X-ray diffraction (Fig. 2). No phase transformation or any impurity was observed after the $BaAl_2O_4$ sample was reduced by H_2 for 2 h at 700 °C. The grain size and crystalline size were approximately the same for both $BaAl_2O_4$ samples, with an average crystalline size of about 40 nm.

Figure 3 shows transmission electron microscopy (TEM) images of the $BaAl_2O_4$ samples before and after (Fig. 3A and 3B, respectively) reduction. The $BaAl_2O_4$ sample prepared at 900 °C for 2 h shows a relatively regular particle shape, and the average grain size is in the range of 80 to 100 nm. After the $BaAl_2O_4$ sample is reduced in H_2 at 700 °C for 2 h, the morphology changed. The edge of the particles becomes dim compared with the unreduced sample, suggesting damage to the

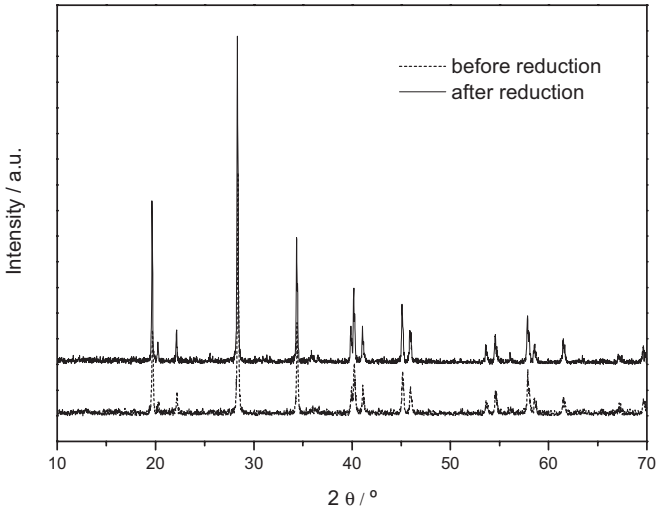

Figure 2. X-ray diffraction patterns of $BaAl_2O_4$ and R-$BaAl_2O_4$ samples.

$BaAl_2O_4$ surface structure. Moreover, the aggregation of the particles becomes more serious, and the particle size is slightly reduced, which can also be attributed to damage to the surface structure in the reduction process. During reduction in H_2, it is easier for the lattice oxygen of $BaAl_2O_4$ in the surface to react with H_2; consequently, oxygen vacancies form in the surface. The formation of oxygen vacancies in the $BaAl_2O_4$ surface results in instability of the $BaAl_2O_4$ particles, which may aggregate to produce an optimized structure, and interface diffusion among particles happens. Thus, after H_2 reduction, the particle size slightly varies, but the morphology of $BaAl_2O_4$ is greatly changed. Oxygen vacancies play an important role in this morphology variation.

Al 2p, O 1s, and Ba $3d_{5/2}$ X-ray photoelectron spectroscopy (XPS) results of the $BaAl_2O_4$ samples before and after reduction are shown in Figure 4A–C, respectively. The Al 2p binding energies are 73.81 and 72.92 eV in the oxide form of $BaAl_2O_4$, which could be characteristic of Al species in AlO_4 tetrahedra

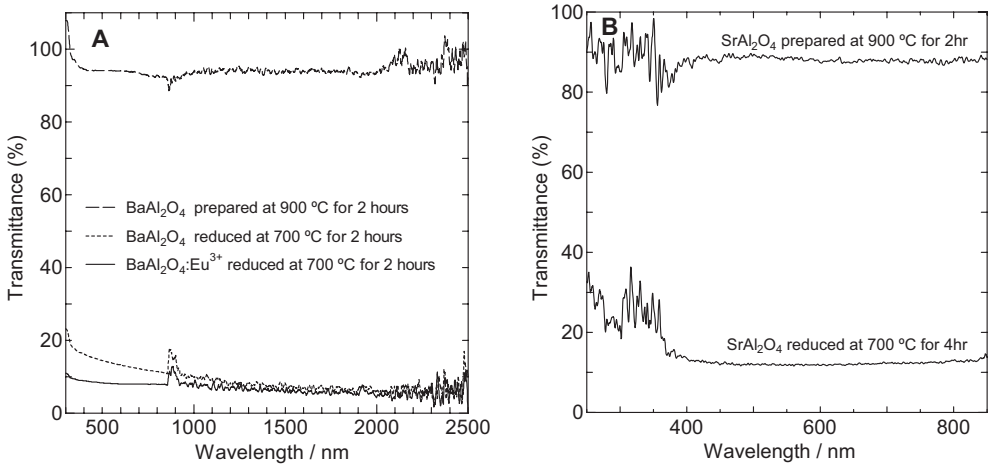

Figure 1. UV-vis spectra of a $BaAl_2O_4$ sample (A) and a $SrAl_2O_4$ sample (B) before and after reduction by H_2.

ADVANCED FUNCTIONAL MATERIALS

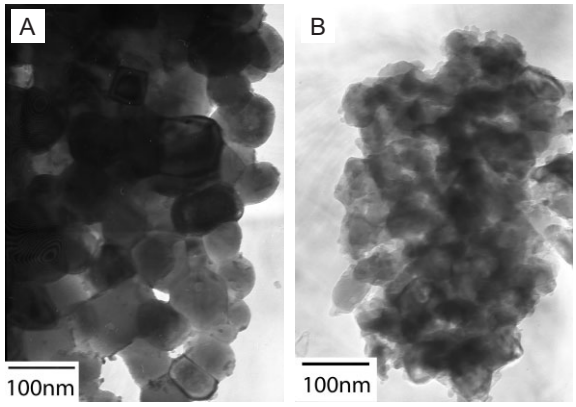

Figure 3. Transmission electron microscopy images of $BaAl_2O_4$ samples before (A) and after (B) reduction.

and oxygen-deficient AlO_4, respectively. After the $BaAl_2O_4$ sample is reduced at 700 °C, the peak in the reduced species at 72.92 eV strongly intensifies, indicating that the surface is essentially dominated by Al^{3+} species after reduction. The binding energy of O 1s in $BaAl_2O_4$ is 531.3 eV, with a big shoulder at 529.9 eV. The binding energy at 531.3 eV could be ascribed to the characteristics of O species in oxide form, while 529.9 eV might be characteristic of O species in surface hydroxyl groups from H_2O molecules absorbed on $BaAl_2O_4$. In the case of R-$BaAl_2O_4$, the peak of the binding energy of 529.9 eV greatly intensifies, which is attributable to the increase of hydroxyl content on the R-$BaAl_2O_4$ surface. Because of the oxygen vacancies in the R-$BaAl_2O_4$ surface, it is much more defected than the surface of $BaAl_2O_4$; as a consequence, more Al atoms with unsaturated coordination exist in the surface, and more surface hydroxyl groups might form in the surface.

Figure 4D shows valence band XPS spectra of $BaAl_2O_4$ samples. The theoretical results have been plotted on a banding energy scale for comparison. The valence band region and the band near the valence band consist of four distinct features labeled a–d, which are in excellent agreement with the theoretical results (see Section 2.4, below). Band a is the valence band, which consists of three features located at 3.6, 5.1, and 7.5 eV. These three bands could be attributed to O 2p, Al 3p, and Al 3s states, respectively. Band b is located at a binding energy of 12.2 eV and is mainly formed by Ba 5p states. Band c around 20 eV can be associated with overlapping O 2s and Al 3s3p states. Finally, feature d with a binding energy at 27.6 eV is composed of Ba 6s. The valence band spectra of $BaAl_2O_4$ before and after reduction show negligible difference.

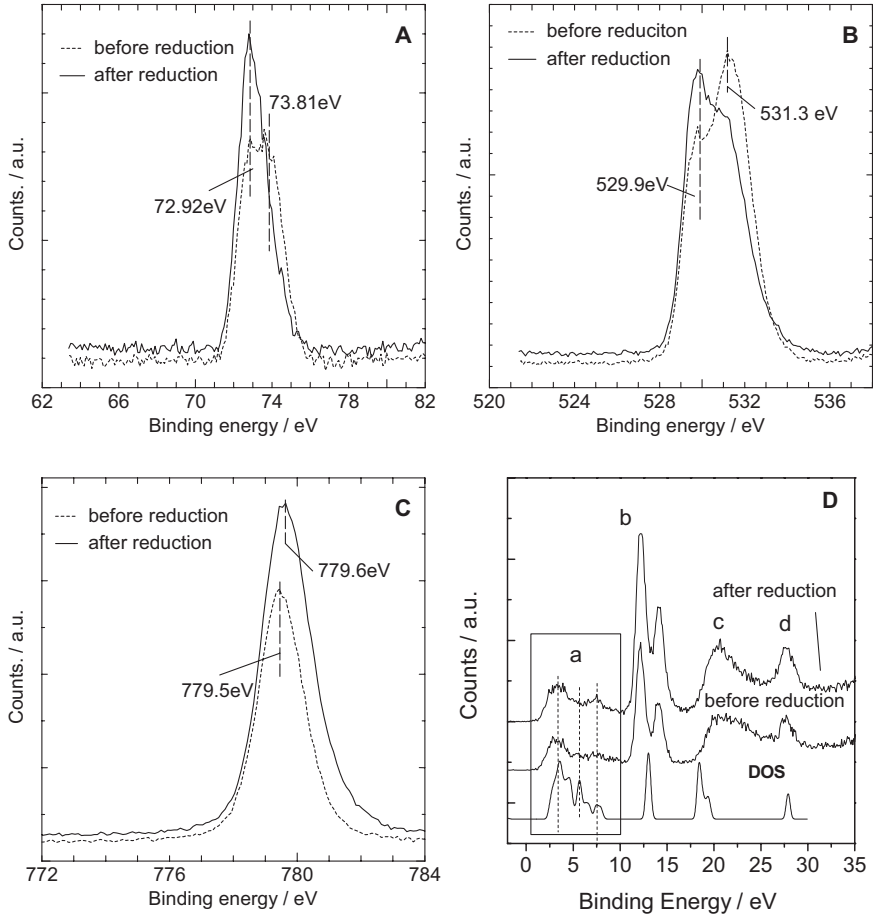

Figure 4. X-ray photoelectron spectra of $BaAl_2O_4$ samples before and after reduction. A–D) Al 2p, O 1s, Ba $3d_{5/2}$, and valence bands (DOS: density of states), respectively. (See text for explanation of a–d features in (D).)

2.3. Formation of Oxygen Vacancies

To investigate the reduction process, temperature-programmed reduction was performed on the $BaAl_2O_4$ sample: the TPR profiles are shown in Figure 5. The TPR profile of $BaAl_2O_4$ samples prepared under various conditions all show a major reduction peak at 860 °C and a minor reduction peak at 580–650 °C. The peak at 860 °C corresponds to the metallic reduction of the $BaAl_2O_4$ sample. The minor peak at 600 °C is related to the partial loss of lattice oxygen atoms, which results in oxygen vacancies in the $BaAl_2O_4$ lattice. The reduction peak becomes weaker with the increase of the calcination temperature of the $BaAl_2O_4$ samples. As the $BaAl_2O_4$ samples used in TPR analysis all weigh in the region of 0.022–0.023 g, it can be concluded that the difference in peak intensity results not from the weight of the samples but from their different capacities for reduction. Generally, when the synthesis temperature of the $BaAl_2O_4$ sample is lower, there are relatively more defects in the $BaAl_2O_4$ sample. The diffusion and reaction of H_2 in the $BaAl_2O_4$

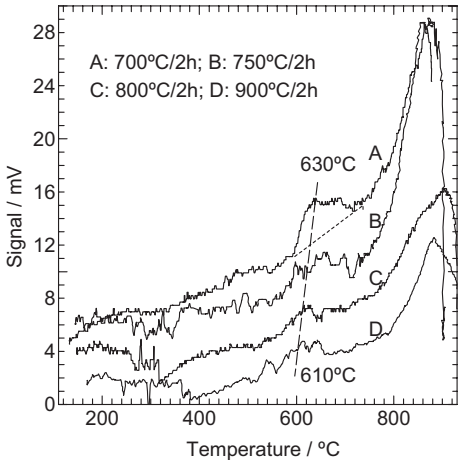

Figure 5. H_2-TPR profile of $BaAl_2O_4$ samples prepared under various temperatures.

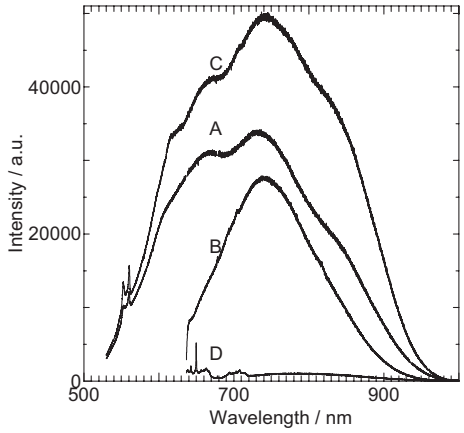

Figure 6. Laser Raman spectroscopy of $BaAl_2O_4$ samples before and after reduction (514 nm laser). A: prepared at 650 °C/4 h and reduced for 2 h; B: prepared at 900 °C/2 h and reduced for 700 °C/2 h; C: Eu^{3+} dopant prepared at 900 °C/2 h and reduced for 700 °C/2 h; D: prepared at 900 °C/2 h.

sample synthesized at a lower temperature is much easier; hence, the reduction peak is much stronger. Quantitative analysis of TPR traces indicates that about 0.464 % oxygen vacancies were formed in $BaAl_2O_4$ prepared at 700 °C based on hydrogen consumption, and the total H_2 consumption is dependent on calcination temperature. The $BaAl_2O_4$ sample calcined at 700 °C for 2 h consumed more H_2 and formed the most oxygen vacancies.

Raman spectra of the $BaAl_2O_4$ samples before and after reduction are shown in Figure 6. Raman spectroscopy of the $BaAl_2O_4$ prepared at 900 °C for 2 h exhibits Raman scattering peaks only; there is no luminescent background. However, for all the samples undergoing a process of H_2 reduction, very strong luminescent backgrounds around 750 nm are observed in the Raman spectra. With the decrease of calcination temperature adopted in the synthesis of $BaAl_2O_4$, the luminescent intensity increases. Many studies have reported that luminescence is closely related to structural defects, such as oxygen vacancies.[16,17] In our work, the as-prepared $BaAl_2O_4$ particles show no luminescent irradiation because of low defect levels in the crystalline structure, whereas the reduced $BaAl_2O_4$ exhibits strong luminescent irradiation, which could be attributed to oxygen vacancies in the oxygen-deficient samples. The luminescence intensifies as the preparation temperature of $BaAl_2O_4$ decreases, indicating more oxygen vacancies exist in the $BaAl_2O_4$ samples synthesized at lower temperature, which is consistent with the TPR results.

Figure 7 shows the whole field scan and local field scan (Fig. 7A and B, respectively) ESR spectra of the $BaAl_2O_4$ samples before and after reduction. Figure 7A does not show any electron paramagnetic signal for the $BaAl_2O_4$ sample before reduction; only the background noise of the equipment is seen. However, an electron paramagnetic resonance signal is observed with different intensity for the R-$BaAl_2O_4$ samples prepared under different reduction conditions. The local field scan on the $BaAl_2O_4$ samples reduced at 700 °C for 0.5 h and 2 h (Fig. 7B) indicates that both samples show signals at around 3430 G. This implies the same type of defect for both samples. The splitting factor values (g) consequently calculated were 2.032 and 2.031, respectively. The 2 h reduction sample shows higher intensity; this is possibly due to higher defect density.

The electron-trapped center at a site of anion vacancy is well-known as an F center (also known as a color center), which has been widely researched in MgO,[25] ZnO,[26] CaO[27]. In most cases, the g values for the paramagnetic centers are expected to show negative g-shifts (the average g value is lower

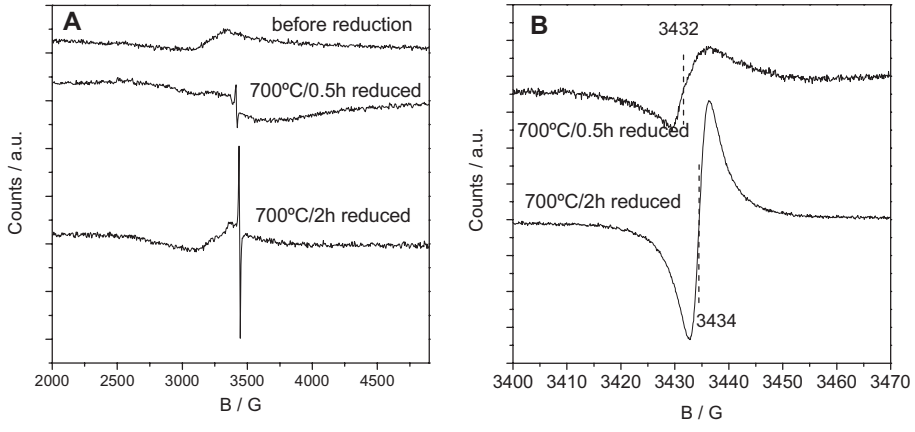

Figure 7. ESR spectra of $BaAl_2O_4$ samples before and after reduction: whole field scan (A) and local field scan (B) (1 G = 10^{-4} Wb m^{-2}).

than free-electron g factor), whereas paramagnetic signals with g values bigger than g_e (positive g-shift), corresponding to oxygen vacancies with a single trapped electron (V_O^+), were observed in defected ZnO,[28–30] TiO_2,[31] and so on. In this work, the electron paramagnetic resonance (EPR) signal might be attributed to the electron-trapped center at the site of oxygen vacancies for the following reasons: a) all the $BaAl_2O_4$ samples, regardless of their reduction degree, are black in color after H_2 reduction (indicative of color-center formation); b) the EPR signal is obviously intensified with the prolonging of the reduction time, indicative of more oxygen vacancy formation; c) it must be taken into account that the reduction was conducted at 700 °C under a flow of H_2 for several hours, so that the oxidation states (paramagnetic) of carbon should be excluded as paramagnetic centers responsible for the EPR signal in the obtained $BaAl_2O_4$ samples; d) the signal should not be caused by impurities: elemental analysis of the $BaAl_2O_4$ samples show that 0.09 % weight ratio of Fe_2O_3 and 0.1 % weight ratio of CaO exist as impurities in the samples. Fe^{3+} and Fe^{2+} can cause paramagnetic signals at g around 2.00;[32,33] however, the low content and the intensification of the EPR signal after reduction indicate the signal should not be related to Fe^{3+} or Fe^{2+}impurities.

The reason for the big g-shift of the EPR signal in the current work is not completely clear. An explanation could be that the existence of complex defect structures (such as neighboring vacancies) might form in R-$BaAl_2O_4$ because of the reduction in the H_2 flow, while no such process was performed in the cases where a small g-shift was observed.[28–31] Further tests need to be done to allow us to draw further conclusions.

2.4. Theoretical Calculations

In order to obtain insight into the special optical properties of the reduced $BaAl_2O_4$ samples, a series of first-principle calculations were performed to assess the influence of oxygen vacancies on the electronic states and optical properties of $BaAl_2O_4$. The plane-wave pseudopotential method[34,35] was used to optimize crystal geometries, to obtain the corresponding electronic band structures, and to simulate the optical absorption spectra. In these calculations, the energy cutoff was chosen at 380 eV. The Brillouin-zone sampling was performed by using a k-grid of $2\times2\times2$ points for the calculations. Ultrasoft pseudopotentials were used for barium, aluminum, and oxygen atoms. The generalized gradient approximation (GGA) with Perdew, Burke and Ernzerhof (PBE) exchange correlation functional was adopted. The presence of oxygen vacancies was modeled by removing oxygen atoms in $BaAl_2O_4$ cells, thus, forming $BaAl_2O_{4-x}$ compounds. We considered removing one, two, or four oxygen atoms from an 80 atom supercell, with corresponding x values of 0.08, 0.16, or 0.32, respectively. Considering that a complex defect structure might exist in $BaAl_2O_{4-x}$ compounds, a model with neighboring oxygen vacancies was built in the case of $BaAl_2O_{4-x}$ ($x=0.32$, four oxygen atoms were removed from the 80 atom supercell), resulting in two groups of adjacent vacancies. Finally, the geometries of all these configurations were fully optimized to an energy minimum.

The space group of $BaAl_2O_4$ is $P6_322$, and the hexagonal phase has a three-dimensional network of corner-sharing AlO_4 tetrahedra, which have channels in the a- and c-directions, where Ba^{2+} ions are located (Fig. 8A and B). The structure is defined by three crystallographic parameters: two lattice parameters, a and c, and the internal parameter, $u=d_{ap}/c$, where d_{ap} is the apical Al–O bond length. The ground-state structure of $BaAl_2O_4$ was obtained by minimizing the total energy. In Table 1, the calculated optimized structure compared with the experimental results are listed. The correlation between the structures as calculated and the experiment is very good with a margin of error below 2 %, which demonstrates the high degree of accuracy of our method. The optimized primitive unit cells of $BaAl_2O_4$ and R-$BaAl_2O_4$ are depicted in Figure 9A and B, respectively. In Table 2, the bond lengths of Al–O and

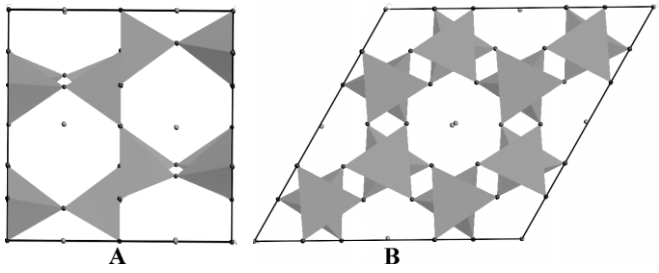

Figure 8. Schematic views of the monoclinic phase of $BaAl_2O_4$ along the a- (A) and c-directions (B). Gray and black spheres represent Ba and O, respectively, and gray show AlO_4 tetrahedra.

Table 1. Optimized structural parameters of $BaAl_2O_4$ compared with experimental values.

	a [Å]	c [Å]	d_{ap} [Å]	c/a	u ($=d_{ap}/c$)	2θ
Experimental	10.449	8.793	1.747	0.842	0.199	114.270°
This work	10.369	8.807	1.718	0.849	0.195	112.386°
Error [%]	0.8	0.2	0.8	0.8	2	1.6

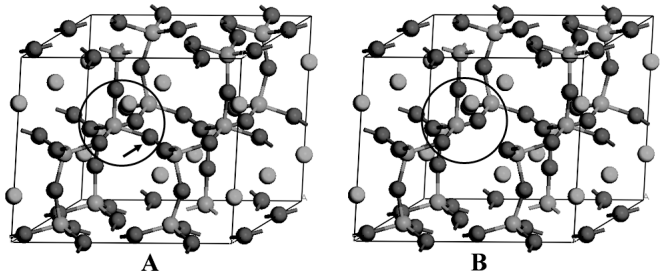

Figure 9. The optimized primitive unit cell of $BaAl_2O_4$ (A) and R-$BaAl_2O_4$ (B). Gray, black and light gray spheres represent Ba, O, and Al atoms, respectively. The O atom pointed to in the circle was removed, creating an oxygen vacancy.

Table 2. The Al–O bond lengths and O–Al–O bond angles within an AlO_4 tetrahedron before and after one oxygen atom is removed.

	Bond lengths [Å]	Bond angles [°]
$BaAl_2O_4$	Al4–O3: 1.723	O3–Al4–O3: 108.814
	Al4–O6: 1.720	O3–Al4–O6: 104.655
R-$BaAl_2O_4$	Al4–O3: 1.738	O3–Al4–O3: 112.229
	Al4–O6: 1.739	O3–Al4–O6: 106.549

the bond angles of O–Al–O within an AlO_4 tetrahedron, before and after one oxygen atom is removed, are shown. The bond lengths of Al–O become longer by about 0.15 Å after one oxygen atom is removed; also the bond angles of O–Al–O become larger, which can be attributed to the coordination of Al in the AlO_4 tetrahedra becoming unsaturated after the oxygen atom is removed.

The electronic density of states for the $BaAl_2O_{4-x}$ crystal is shown in Figure 10. The bandgap is about 4.5 eV, which underestimates the experimental value, a well-known tendency of density functional theory calculations. At the top of the valence band, in the region between –6 and 0 eV, O 2p states hybridize mostly with Al 3p orbitals, and to a lesser extent with an admixture of Al 3s and Ba 5d states. The conduction band (CB), just above the Fermi level (E_F), is primarily governed by the unoccupied Ba 5d states. Compared with the perfect $BaAl_2O_4$ crystal, the density of states curves for the oxygen vacancy show that a small peak occurs within the forbidden band at 1.68 eV when $x = 0.08$. As the vacancy concentration increases, the impurity states become broader and more intensified. The width of the impurity states is about 0.8, 1.7, and 2.9 eV for $x = 0.08$, 0.16, and 0.32, respectively. As $x = 0.32$, where adjacent vacancies are considered, the impurity state is split into two parts. The impurity state is mainly formed from Al 3p orbitals. This state is fully occupied because the oxygen vacancy removes six oxygen p states from the valence band while removing only four valence electrons, leaving two extra electrons, which can be accommodated by the AlO_3 group. The impurity state is about 1.0 eV above the valence-band edge, which correlates with the concentration of oxygen vacancies.

Since the electronic structure is calculated, the transition rates between occupied and unoccupied states caused by the interaction with photons were determined. The imaginary part of the dielectric constant can be described as a joint density of states between the valence and conduction bands. Thus, the absorption curves can be obtained easily from the imaginary part of the dielectric constant. The scissors operator of 0.5 eV was introduced to shift all the conduction levels to agree with the experimental value of the bandgap. The calculated optical absorption spectra are shown in Figure 11. For a relatively high vacancy concentration ($x = 0.16$), the large contribution to the electron transitions from the donor states results in optical absorption from 250 to 600 nm. Lower vacancy concentrations results in less optical absorption; in other words, the absorption region is narrower. It is notable that when adjacent oxygen vacancies exist in $BaAl_2O_{4-x}$ ($x = 0.32$), optical absorption is much more broadened. A calculated wide-spectra optical absorption from 250 to 1100 nm is observed in the case of $BaAl_2O_{4-x}$ ($x = 0.32$). Therefore, the optical properties of R-$BaAl_2O_4$ significantly depend on the oxygen-vacancy concentrations and the defect structure.

2.5. Discussion of the Optical Properties of R-$BaAl_2O_4$

Based on the TPR analysis, the oxygen-vacancy concentration in R-$BaAl_2O_4$ is about 0.464 %; accordingly, the value of x in $BaAl_2O_{4-x}$ is evaluated to be 0.02. Although this value is smaller than the theoretical model calculations ($x = 0.08$ and 0.16), as oxygen vacancies concentrate in the surface of R-$BaAl_2O_4$, the value of x in the surface could be much bigger than 0.02. Based on TEM images, it can be speculated that oxygen vacancies mainly exist in the surface of $BaAl_2O_4$, with a depth of ca. 1–2 nm. If so, the value of x can be roughly estimated: based on the supposition that $BaAl_2O_4$ particles have a sphere morphology with a diameter of 40 nm, x could be evaluated as about 0.14. Although this value is still less than 0.16, the irregular distribution of oxygen vacancies at the surface and the irregularity of the morphology of $BaAl_2O_4$ should affect the value of x in the surface. In theoretical calculations, the defected $BaAl_2O_4$ is modeled by removing one or more oxygen atoms from the $BaAl_2O_4$ cell. However, the situation seems to be much more complicated in reality. The theoretical study could provide us with a better understanding of what happens after one or more oxygen atoms are removed. It is known from theoretical calculations that impurity states form in the forbidden band of $BaAl_2O_4$, the introduced oxygen vacancy could enhance and expand the optical absorption of $BaAl_2O_4$, and the enhanced optical absorption significantly depends on the concentration of the oxygen vacancies.

To understand the special optical absorption of R-$BaAl_2O_4$, several factors must be taken into consideration: 1) the particle size of R-$BaAl_2O_4$; 2) anti-structure disorders in R-$BaAl_2O_4$, including the possibility of complex defect structures (such as neighboring vacancies), the concentration and the chemical state of oxygen vacancies; 3) the difference in physical properties of $BaAl_2O_4$ compared with other compounds (such as TiO_2, $PbWO_4$, etc.), in which no similar optical property is observed after the same treatment.

The particle size is an important factor that affects the optical absorption of R-$BaAl_2O_4$. This special optical behavior was not observed in an experiment in which micrometer-sized $BaAl_2O_4$ (particle size about 3 μm) was used as the starting material (see Supporting Information). The $BaAl_2O_4$ particles involved in the present work were nanometers in size, which played an important role in the ultimate surface structure of R-$BaAl_2O_4$. Surface effects and small-size effects are characteristics of nanometer-sized particles. Because of these characteristics in nanometer-sized $BaAl_2O_4$, the fraction of surface atoms increases, and the surface is much more active. Consequently, after the same period of H_2 reduction, nanometer-sized $BaAl_2O_4$ contains more oxygen vacancies in the surface. Moreover, based on TPR analysis of $BaAl_2O_4$ samples synthesized at different temperatures, oxygen-vacancy concentration formed by reduction was found to be closely related to the cal-

ADVANCED FUNCTIONAL MATERIALS

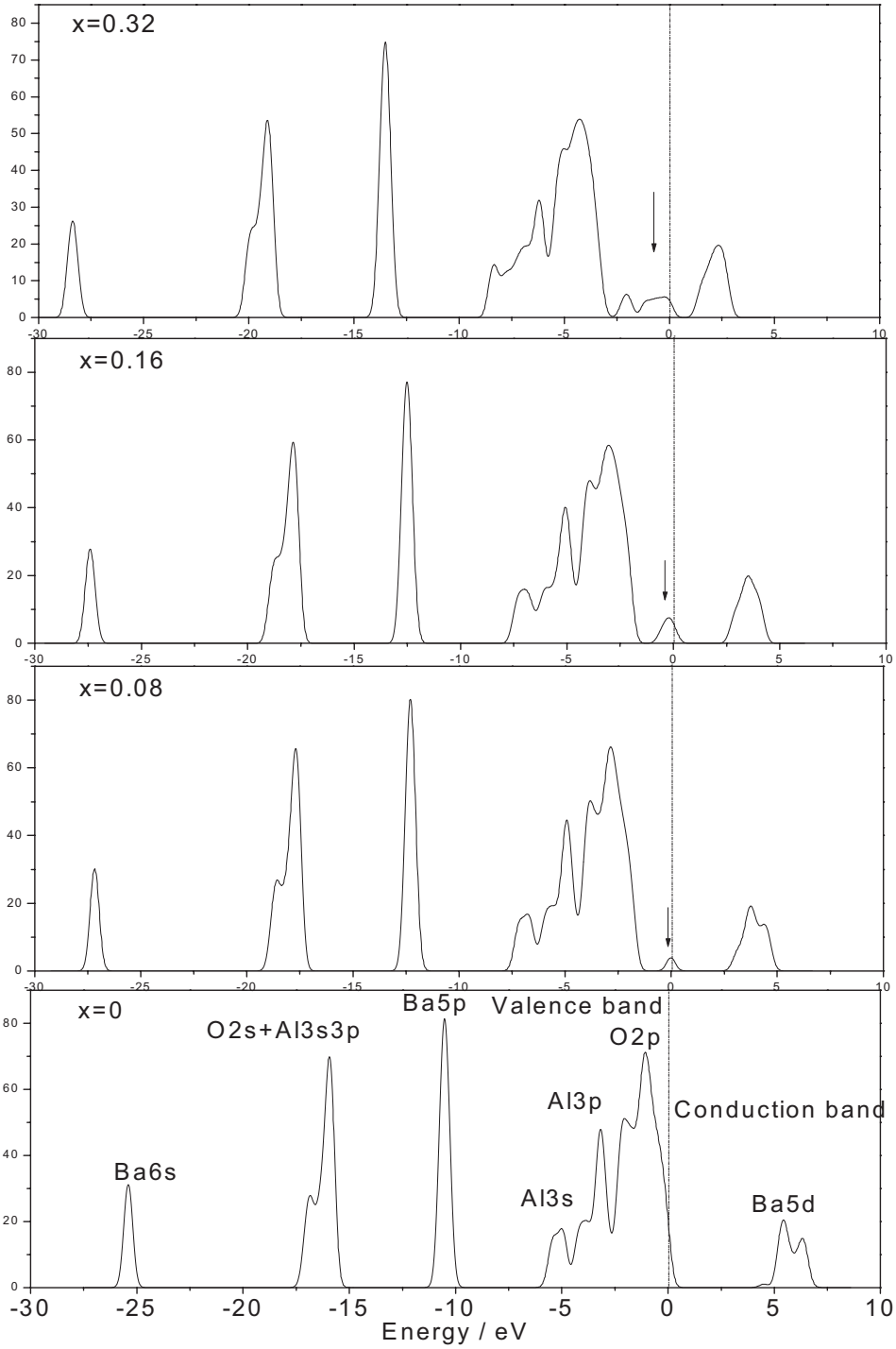

Figure 10. Density of states with respect to the concentration of oxygen vacancies in the $BaAl_2O_{4-x}$ crystal.

cination temperatures of $BaAl_2O_4$. Generally, to acquire micrometer-sized $BaAl_2O_4$, a higher temperature (1200 °C in our work) is needed during formation. So, for micrometer-sized $BaAl_2O_4$, it seems relatively more difficult to form oxygen vacancies during H_2 reduction than it is for nanometer-sized $BaAl_2O_4$. As the optical properties of reduced $BaAl_2O_4$ significantly depend on the oxygen-vacancy concentration, micrometer-sized R-$BaAl_2O_4$ has different optical absorption behavior.

There have been numerous studies of the surfaces of insulating metal oxides in an attempt to clarify the type of defect sites that can exist.[36–39] The most common defects are coordinatively unsaturated ions caused by the presence of planes, edges, corners, anion/cation vacancies, and electron-excess centers. Before proceeding to an examination of the optical results, it is helpful to consider the structure of $BaAl_2O_4$ and the probable nature of native imperfections. The two types of cation sites,

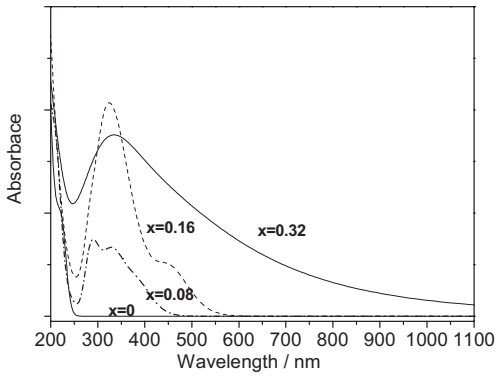

Figure 11. Calculated optical absorption spectra of $BaAl_2O_4$ with different oxygen-vacancy concentrations.

with their distinctive octahedral and tetrahedral coordination, provide for a greater variety of defects than either BaO or Al_2O_3, both of which exhibit essentially octahedral coordination. Local neutrality is maintained when the tetrahedral site is occupied by a divalent cation and the octahedral site is occupied by a trivalent ion. Hence, site mixing by the two types of cation results in local charge concentration, which could lead to trapping of charge carriers: A Ba^{2+} on an Al^{3+} site is a site deficient in positive charge, which should serve as a hole trap, whereas the converse would hold for an Al^{3+} on a Ba^{2+} site. In the present work, $BaAl_2O_4$ was prepared via annealing of a polymerization complex precursor, and so extensive cation-site mixing is expected. It is also possible to have nonstoichiometry involving any of the three constituents. It has been shown that oxygen can be extracted by heating in a H_2 atmosphere. This treatment results in oxygen vacancies populated with one or two electrons. Since the cations possess only one chemically stable valence state, charge compensation for the oxygen vacancies is accomplished by transferring extra electrons to them in the reducing atmosphere. Alternatively, nonstoichiometry can result from extra molecules of BaO or Al_2O_3 in the composition with no need for electrons (or holes) to preserve neutrality. Under such conditions, charge compensation would be accomplished by the introduction of oxygen vacancies in the case of BaO excess and Ba vacancies for excess Al_2O_3. X-ray fluorescence measurements on our samples have shown that excess Al^{3+} ions replaced Ba^{2+} ions with $x \approx 1.01$ ($BaAl_2O_4$ seen as BaO:$x$$Al_2O_3$). The existence of various defects and the possibility of a complex defect structure could affect the optical properties of $BaAl_2O_4$.

Additionally, it is important to note that the character of the impurity state introduced by oxygen vacancies in this work is different from the widely researched oxygen vacancies in TiO_2, $PbWO_4$, and so on. In those cases, the impurity state is just below the conduction band, sometimes even overlapping with the conduction band.[14–16] In the present work, the impurity state is above the valence band and deep in the bandgap. We attribute this difference to the composition of the impurity states and the conduction bands. Generally, for a compound with a composition of $A_xB_yO_z$, the valence band is mostly composed of O 2p orbitals, while the conduction band can be formed from either the s orbital of element A or the d orbitals of element B. These two kinds of conduction band structures may affect the composition of the impurity states introduced by the oxygen vacancies. In the present work, the conduction of $BaAl_2O_4$ is composed mainly of Ba 5s, while the impurity state is associated with the AlO_4 group. By contrast, in the case of $PbWO_4$, the conduction band consists primarily of W 5d, while the impurity is also formed from W 5d. It is found that the conduction band and impurity states are formed from two different elements in insulator $BaAl_2O_4$, while the conduction band or impurity states both consist of W 5d in the case of $PbWO_4$.

To clarify that the carbon materials (such as amorphous carbon, graphitic carbon) are not responsible for the observed blackening of the reduced $BaAl_2O_4$ samples, the possible content of carbon materials was investigated by thermogravimetric analysis (TGA) and differential thermal analysis (DTA). The results for the $BaAl_2O_4$ sample reduced at 700 °C for 2 h are shown in Figure 12. It is clearly shown that negligible weight loss is observed from 80 to 1000 °C in a flow of air, indicating

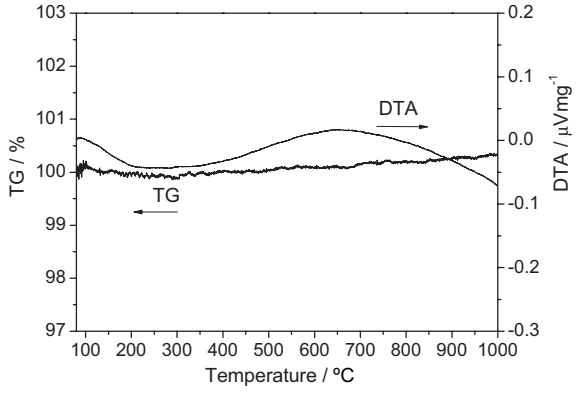

Figure 12. The TGA and DTA spectra of the $BaAl_2O_4$ sample reduced at 700 °C for 2 h.

that a high content of carbon materials is impossible in the reduced $BaAl_2O_4$ sample. Therefore, the carbon materials could be excluded as a reason for the observed blackening of the reduced $BaAl_2O_4$ samples. It is notable that the weight increases in the region from 400 to 1000 °C, and an exothermic peak is observed around 650 °C. These observations might be related to the restoration of oxygen vacancies in the reduced $BaAl_2O_4$ sample.

Additionally, other possible carbon species (carbonate or other oxidation states of carbon) were examined by XPS and Fourier transform IR (FTIR) spectroscopy (see Supporting Information). It can be concluded that carbon mainly exists as carbonate in both the $BaAl_2O_4$ and R-$BaAl_2O_4$ samples. The carbonate changes slightly after $BaAl_2O_4$ is reduced, indicating that the carbonate should not be the reason for the blackening of $BaAl_2O_4$.

ADVANCED FUNCTIONAL MATERIALS

3. Conclusions

$BaAl_2O_4$ with oxygen vacancies shows very strong optical absorption in the spectral region from 200 to 2500 nm. Both theoretical and experimental evidence show that the impurity state in the forbidden band induced by oxygen vacancies is the main reason for this enhanced photoabsorption. The optical properties of R-$BaAl_2O_4$ significantly depend on the oxygen-vacancy concentration. Other factors, such as particle size, complex vacancy structure, and electronic structure of $BaAl_2O_4$ are all responsible for the strong optical absorption in this wide range of wavelength.

4. Experimental

4.1. Synthesis of $BaAl_2O_4$ and R-$BaAl_2O_4$

Firstly, fresh $Al(OH)_3$ was prepared by dropping $NH_3 \cdot H_2O$ into an $Al(NO_3)_3$ solution followed by several washings using centrifugation. Then H_5DTPA (diethylenetrianminepentaacetic acid) solution was mixed with fresh $Al(OH)_3$ and $Ba(OH)_2$ in a calculated molar ratio, heated, and stirred with a magnetic stirrer to promote the formation of a heteronucleus complex. After the solution became transparent, it was dried at 60–80 °C to yield the precursor. $BaAl_2O_4$ was synthesized by calcining the precursor in air. A slow heating rate (5 °C min^{-1}) was used to increase the temperature to various pre-set temperatures and maintained for a defined period of time to promote the formation of $BaAl_2O_4$.

Reduction of $BaAl_2O_4$ was accomplished in hydrogen at temperatures of the order of 700–900 °C and times of several hours. Reduced samples were subsequently cooled in argon to prevent reoxidation.

4.2. Characterization

The purity and crystallinity of the as-prepared sample was characterized by a X-ray power diffraction (XRD) on a Bruker D8-advance X-ray diffractometer operated at 40 kV and 20 mA using a Cu Kα ($\lambda = 1.5418$ Å) radiation source. XRD data for indexing and cell-parameter calculation were collected in a scan mode with a step length of 0.02° and a preset time of 3 s per step. The average crystal size of $BaAl_2O_4$ powder samples was calculated with the Scherrer equation: $D_c = K\lambda/\beta\cos\theta$, where D_c is the average crystal size, K is the Scherrer constant (0.89), λ is the X-ray wavelength (0.15418 nm), β is the full width at half-maximum (FWHM), and θ is the diffraction angle. The peak at 28.3° was used for the calculation of the crystal size. The morphologies and structures of the prepared samples were further examined by TEM. Images at low magnification were obtained on a JEOL JEM-1010 instrument operated at an accelerating voltage of 120 kV. Diffuse reflection spectra were obtained on a Hitachi U-3010 UV-Vis spectro-photometer. The Raman spectra were measured under a microscope using a 20× objective to focus the incident excitation laser radiation into a spot diameter of either 1–2 or 2–3 μm and to collect the scattered light. The laser power was kept low enough, to avoid heating of the samples, by optical filtering or defocusing of the laser beam at the sample surface. Spectra were collected in the range of 1000–200 cm^{-1} with a resolution of 1 cm^{-1}. X-ray photoelectron spectroscopy (XPS) spectra were measured in a PHI 5300 ESCA system. An Al Kα X-ray source with a power of 250 W was used. The pass energy of the analyzer was set at 37.25 eV, and the base pressure of the analysis chamber was better than 4×10^{-8} Torr (1 Torr = 133.3 Pa). The charge effect was calibrated using the binding energy of C 1s. Temperature-programmed reduction (TPR) results were obtained by using a Micromeritics apparatus. Samples of 22 mg were first treated in argon at 673 K for 1 h, cooled to room temperature, and subsequently contacted with a H_2/Ar mixture (molar ratio of 0.15 and a total flow rate of 3 L h^{-1}). The samples were heated at a rate of 10 K min^{-1} to a final temperature of 1273 K. Electron paramagnetic resonance (EPR) spectra were recorded on a Bruker ER-200 spectrometer working in the X-band and calibrated with a DPPH (a′-diphenyl-b-picrylhydrazyl) standard ($g = 2.0036$). Portions of ca. 30 mg of sample were introduced into an ESR quartz probe cell and handled in a conventional high-vacuum line for the different treatments. In all cases, the samples were extensively outgassed at room temperature prior to recording spectra. TGA–DTA analyses were performed on a Dupont 1090 thermal analyzer, the atmosphere was air, and the heating rate was 5 °C min^{-1}. Infrared transmission spectra were recorded for KBr disks containing the powdered sample with an FTIR spectrometer (Perkin–Elmer 1600).

Received: May 5, 2007
Revised: August 4, 2007
Published online: November 7, 2007

[1] a) M. Emmelius, G. Pawlowski, H. W. Vollmann, *Angew. Chem. Int. Ed. Engl.* **1989**, *28*, 1445. b) S. Sengupta, S. K. Sadhukhan, *J. Chem. Soc., Perkin Trans. 1* **2000**, 4332. c) J. Fabian, I. L. Nakamura, M. Matsuoka, *Chem. Rev.* **1992**, *92*, 1197. d) A. Tsuda, A. Osuka, *Science* **2001**, *293*, 79. e) *Infrared Optical Circuits and Components: Design and Applications* (Ed: E. J. Murphy), Marcel Dekker, New York **1999**. f) P. Chandrasekhar, B. J. Zay, G. C. Birur, S. Rawal, E. A. Pierson, L. Kauder, T. Swanson, *Adv. Funct. Mater.* **2002**, *12*, 95. g) D. A. Jose, A. D. Shukla, K. Kumar, B. Ganguly, A. Das, G. Ramakrishna, D. K. Palit, H. N. Ghosh, *Inorg. Chem.* **2005**, *44*, 2414.

[2] M. D. Ward, J. A. McCleverty, *J. Chem. Soc., Dalton Trans.* **2002**, 275, and references therein.

[3] U. T. Mueller-Westerhof, B. Vance, D. I. Yoon, *Tetrahedron* **1991**, *47*, 909, and references therein.

[4] a) A. M. Barthram, R. L. Cleary, R. Kowallick, M. D. Ward, *Chem. Commun*. **1998**, 2695. b) J. G. Canadas, A. P. Meacham, L. M. Peter, M. D. Ward, *Angew. Chem. Int. Ed.* **2003**, *42*, 3011.

[5] I. M. Blake, L. H. Rees, T. D. W. Claridge, H. L. Anderson, *Angew. Chem. Int. Ed.* **2000**, *39*, 1818, and references therein.

[6] a) H. S. Cho, D. H. Jeong, S. Cho, D. Kim, Y. Matsuzaki, K. Tanaka, A. Tsuda, A. Osuka, *J. Am. Chem. Soc*. **2002**, *124*, 14 643. b) A. D. Shukla, H. C. Bajaj, A. Das, *Angew. Chem. Int. Ed.* **2001**, *40*, 446.

[7] V. Melissa , L. T. Michel, M. A. David, *Adv. Mater.* **2000**, *12*, 337.

[8] J. Isaac, O. Pablo, C. Gabriel, L. M. José, F. Jordi, A. B. Giovanni, G. Rosalba, F. Albert, *Adv. Mater.* **2002**, *14*, 1399.

[9] B. Emanuele, M. C. Anna, K. Iskandar, P. Paolo, P. Alessandro, M. Paolo, C. Cinzia, S. Omar, M. Roberto, S. Massimo, *Adv. Mater.* **2005**, *17*, 1842.

[10] J. M. Li, *Appl. Phys. Lett.* **1989**, *55*, 2223.

[11] J. Isaac, O. Pablo, C. Gabriel, L. M. José, F. Jordi, A. B. Giovanni, G. Rosalba, F. Albert, *Adv. Mater.* **2002**, *14*, 1399.

[12] L. E. Halliburton, N. C. Giles, N. Y. Garces, M. Luo, C. Xu, L. Bai, L. A. Boatner, *Appl. Phys. Lett.* **2005**, *87*, 172 108.

[13] Y. B. Abraham, N. A. W. Holzwarth, R. T. Williams, G. E. Matthews, A. R. Tachett, *Phys. Rev. B* **2001**, *64*, 245 109.

[14] D. C. Cronemeyer, *Phys. Rev.* **1959**, *113*, 1222.

[15] Z. S. Lin, A. Orlov, R. M. Lambert, M. C. Payne, *J. Phys. Chem. B* **2005**, *109*, 20 948.

[16] A. T. Paxton, L. Thiên-Nga, *Phys. Rev. B* **1998**, *57*, 1579.

[17] T. H. Stokes, C. Sadate, M. D. Hatch, L. L. Boyer, J. M. Mehl, *Phys. Rev. B* **2002**, *65*, 064 105-1.

[18] S. Y. Huang, V. D. Mühll, J. Ravez, P. Hagenmuller, *J. Phys. Chem. Solids* **1994**, *55*, 119.

[19] A. A. Bush, G. A. Laptev, *Sov. Phys.—Solid State* **1989**, *31*, 535.

[20] T. Ion, N. Ciocea, *Cemento* **1980**, *77*, 3.

[21] M. M. Ali, K. S. Agarval, K. S. Handoo, *Cem. Concr. Res.* **1995**, *25*, 86.

[22] G. Blasse, A. Bril, *Philips Res. Rep.* **1968**, *23*, 201.

[23] S. H. M. Poort, W. P. Blokpoel, G. Blasse, *Chem. Mater.* **1995**, *7*, 1547.
[24] C. A. Zhang, L. Wang, L. P. Cui, Y. F. Zhu, *J. Cryst. Growth* **2003**, *255*, 317.
[25] D. M. Murphy, R. D. Farley, I. J. Purnell, C. C. Rowlands, A. R. Yacob, *J. Phys. Chem. B* **1999**, *103*, 1944.
[26] N. G. Kakazev, T. V. Sreckovic, M. M. Ristic, *J. Mater. Sci.* **1997,** *32*, 4619.
[27] M. Chiesa, M. C. Paganini, E. Giamello, D. M. Murphy, *Langmuir* **1997**, *13*, 5306.
[28] B. Yu, C. Zhu, F. Gan, Y. Huang, *Mater. Lett.* **1998**, *33*, 247.
[29] L. Jing, Z. Xu, J. Shang, X. Sun, W. Cai, H. Guo, *Mater. Sci. Eng. A* **2002**, *322*, 356.
[30] V. Ischenko, S. Polarz, D. Grote, V. Stavarache, K. Fink, M. Driess, *Adv. Funct. Mater.* **2005**, *15*, 1945.
[31] T. Ihara, M. Miyoshi, M. Ando, S. Sugihara, Y. Iriyama, *J. Mater. Sci.* **2001**, *36,* 4201.
[32] E. S. Kirkpatrick, K. A. Müller, R. S. Rubins, *Phys. Rev.* **1964**, *135*, A86.
[33] G. R. Hertel, H. M. Clark, *J. Phys. Chem.* **1961**, *65*, 1930.
[34] M. C. Payne, M. P. Teter, D. C. Allan, T. A. Arias, J. D. Joannopoulos, *Rev. Mod. Phys.* **1992**, *64*, 1045.
[35] M. D. Segall, P. J. D. Linda, M. I. J. Probert, C. J. Pickard, P. J. Hasnip, S. J. Clark, M. C. Payne, *J. Phys. Condens. Matter* **2002**, *14*, 2717.
[36] H. Liu, L. Feng, X. Zhang, O. Xue, *J. Phys. Chem.* **1995**, *99*, 332.
[37] K. Tanabe, *Solid Acids and Bases*, Academic Press, San Diego, CA **1970**.
[38] M. Utiyama, H. Hattori, K. Tanabe, *J. Catal.* **1978**, *53*, 237.
[39] R. M. Morris, K. J. Klabunde, *Inorg. Chem.* **1983**, *22*, 682.